Terminal and Bridging Fluorine Ligands in TiF$_4$ as Studied by ^{19}F NMR in Solids

Miwa Murakami [a*], Yasuto Noda [b], and K. Takegoshi [b]

[a]Office of Society-Academia Collaboration for Innovation, Kyoto University, Gokasho, Uji, Kyoto, 611-0011, Japan.

[b]Graduate School of Science, Kyoto University, Kitashirakawa Oiwakecho, Sakyo-ku, Kyoto, 606-8502, Japan.

[*] email m-murakami@saci.kyoto-u.ac.jp

Gokasho, Uji, Kyoto 611-0011, Japan

Tel: +81-774-38-4967, Fax: +81-774-38-4996

Abstract :

To examine bonding nature of fluorine ligands in a metal coordinated system, ^{19}F high-resolution solid-state NMR has been applied to TiF_4, which bears both bridging and terminal fluorines. Observed 12 isotropic signals are assigned to 12 crystallographically different fluorines (6 terminal and 6 bridging fluorines) in TiF_4 by referring to the calculated isotropic shifts using density functional theory (DFT). The isotropic chemical shift (δ_{iso}) for terminal F (F_T) appears at high frequency (420~480 ppm from $\delta(CCl_3F) = 0$ ppm) with large shielding anisotropy $\Delta\sigma \sim 850$ ppm. Whereas the δ_{iso} and $\Delta\sigma$ values for bridging F (F_B) are moderate; $\delta_{iso} \sim 0~25$ ppm and $\Delta\sigma \sim 250$ ppm. The origin of the observed high-frequency shift for F_T is ascribed to the second-order paramagnetic shift with increased covalency, shorter Ti-F bonds, and smaller energy difference between the occupied and vacant orbitals. Examination of the orientation of the shielding tensor relative to the molecular structure shows that the most deshielded component of the shielding tensor is oriented along the Ti-F bond. The characteristic orientation is consistent with a Ti-F σ bond formed by d_{YZ} of Ti and p_z of F. Further, we show that the selectively observed spinning sideband patterns and the theoretical patterns with the calculated $\Delta\sigma$ and η (shielding asymmetry) values are not consistent with each other for F_B, indicating deficiency of the present DFT calculation in evaluating $\Delta\sigma$.

1. INTRODUCTION

In various fluorine-containing coordination complexes with transition metals, fluorine acts as a bridging ligand between two metals. For example, in a dimeric species ($M_2F_2L_6{}^{2+}$; M = Co(II) and Cu(II) and L denotes another ligand), two ML_3 units are connected by two bridging fluorines (abbreviated to F_B here) to form trigonal bipyramidal or square pyramidal structures [1]. A tetrameric species ($M_4F_4L_{12}{}^{4+}$; M = Mn(II), Co(II), Ni(II), and Cd(II)) consists of four ML_3 units at the alternating corners of a cubic connected with each other via three F_B atoms at the remaining corners to form the octahedral MF_3L_3 structure. A chain-type compound has the octahedral MF_4L_2 structural unit as the repeating unit with the four fluorines shared by neighboring units. Other important structural types of transition metal fluoro-compounds and fluoride salts are reviewed by Leblanc et al. [2].

In addition to the F_B species, a terminal fluorine (abbreviated to F_T here) has also been long known, and chemical nature of the F_B and F_T species has been investigated. As for a few examples, Reinen et al. have examined the binding properties of F_B and F_T in $M(III)L_6$ complexes (M = Cr(III), Fe(III), and Mn(III)) by a combined vibronic coupling and angular overlap analysis with DFT calculations [3]. It was concluded that the total bond strength and the ionic contributions to the bond energy are $F_T \gg F_B$, and F_B induces much stronger π-bonds than F_T does. A high electrostatic Dy-F_T bond was also shown by high-resolution luminescence spectroscopy and correlated with the single-molecule magnet behavior through experimental magnetic susceptibility data and ab initio calculations, leading a large axial crystal-field splitting of the $J = 15/2$ ground state [4]. It was also shown that the F$^-$ ligands in Cu(II)-F_T in dinuclear Cu(II) complexes based on a diazecine ligand behave as "acceptors" for hydrogen bonding [5].

Among these, we are particularly interested in the reported low-frequency ^{19}F isotropic NMR chemical shift of F_T in a palladium (II) fluoride complexes with an anionic fluoro-substituted diarylamido/bis(phosphine) pincer as a ligand [6]. The chemical shift is -414.3 ppm in C_6D_6 from $\delta(CFCl_3)$ = 0 ppm, which appears to be at the low-frequency end of the range of chemical shifts for metal fluorides. The low-frequency shift was related to the nature of the ligand trans to the fluorine.

Among various fluorine-containing coordination complexes with transition metals, fluorine-titanate(IV) complexes are known to form various supramolecular crystal assembly, which is recently reviewed by Davidovich [7]. In this work, we chose to examine TiF$_4$, which bears both F_T and F_B [8], by ^{19}F high-resolution solid-state NMR. Both isotropic chemical shift (δ_{iso}) and chemical shift anisotropy (CSA) of ^{19}F for F_T and F_B are of concern.

We show that, by employing a high magnetic field of 14 T with fast magic-angle spinning (MAS) (the MAS spinning frequency ν_R = 50 kHz), highly resolved 12 signals for all crystallographically different 12 F sites are obtained. The 12 isotropic chemical shifts are then assigned to the 12 fluorines with the aid of quantum-chemical calculation. The observed isotropic shifts linearly correlated well with those calculated ones. The large high-frequency shift observed for F_T is discussed on the basis of the covalency/ionicity of the Ti-F bonding and the Ti-F bond distance. The calculated ^{19}F shielding anisotropy $\Delta\sigma$ values are anomalously large for F_T (ca. 1000 ppm) and the lowest-frequency (the most shielded) component of the shielding tensor lies along the Ti-F bond direction. This orientation of the shielding tensor is used to consider the molecular orbitals responsible for the Ti-F bonding. Further, the individual spinning-sideband pattern for each fluorine is selectively observed by using the

rotation-synchronized Delays Alternating with Nutation for Tailored Excitation (rs-DANTE [9]). By comparison among the selectively observed sideband patterns and the calculated ones, we show that the experimental $\Delta\sigma$ values are much smaller than those calculated especially for F_B.

2. Experimental Section

TiF_4 was purchased from Sigma-Aldrich Chemistry and used without further purification. The TiF_4 powder sample was sealed into a 1.2 mm NMR MAS rotor in a dry Ar atmosphere.

Most of the NMR measurements were made using a JEOL ECA600 NMR spectrometer at 14 T. The field dependence of the ^{19}F spectrum was observed at 4.7 and 7 T using a homemade NMR system based on the OPENCORE spectrometer [10]. All measurements were done with the same triply-tuned MAS probe (Phoenix NMR) for a 1.2 mm rotor. The resonance frequencies for ^{19}F were 564.8 MHz, 282.8 MHz, and 188.4 MHz for 14 T, 7 T, and 4.7 T, respectively. The ^{19}F MAS spectra were observed by using the Hahn echo sequence under the MAS spinning frequency (ν_R) of 50 kHz. The $\pi/2$ and π pulse lengths were 1.4 μs and 2.62 μs for 14 T, 0.6 μs and 1.25 μs for 7 T, and 1 μs and 1.8 μs for 4.7 T. For separation of the spinning-sideband pattern for each F site, we adopted rs-DANTE at ν_R = 46 kHz and 14 T. The pulse length (t_p) and the number of the short pulse for rs-DANTE were 0.5 μs and 33, respectively. The pulse spacing (Δ) was set as $\Delta = 1/\nu_{MAS} - t_p$, which is 21.2 μs in this work. The three principal values of the chemical-shift tensor (δ_{11}, δ_{22}, δ_{33}) for each F site were deduced from its

spinning-sideband pattern by using the spectral fitting program "dmfit" [11]. The definition of the principal components is as follows:

$$| \delta_{33} - \delta_{iso} | \geq | \delta_{11} - \delta_{iso} | \geq | \delta_{22} - \delta_{iso} |, \qquad (1)$$

The ^{19}F chemical shifts were calibrated in ppm relative to CCl_3F adopting the ^{19}F chemical shift for neat C_6F_6 (-163 ppm [12]) as an external reference.

For calculation of the spinning sideband pattern for given CSA parameters, we used a home-made program based on the multistep method: one rotor period is divided into 200 segments during which the Hamiltonian is assumed to be time-independent. The equation of motion for each duration is solved by diagonalizing the time-independent Hamiltonian. A total 512 real and imaginary components of transverse magnetization were calculated at every 5 segments, and the resulting FID signal was Fourier-transformed after application of 800 Hz exponential broadening. The number of orientations for powder averaging was 39384 (c48u1641 in Ref. [13]).

The ^{19}F magnetic shielding was examined by the DFT calculation with the GIPAW method [14] implemented in CASTEP [15] (BIOVIA Material Studio 2018). The Perdew, Burke, and Ernzerhof (PBE) functional in the generalized gradient approximation (GGA) was used to approximate the exchange-correlation energy with ultrasoft pseudopotential descriptions of the core-valance interactions. The k-points used were 1×4×1. Most of the parameters and settings for calculation were the default ones except for the cut-off energy for the plane wave basis set. Dependence of the calculated NMR parameters on the cut-off energy is given in the Supplementary data (Figure S1), which indicates that more than 600 eV is desirable. In this work, we adopted 750 eV. Geometry optimization was done for fraction of atomic position with the following constraints (1) fixed symmetry, and (2) no rescaling of lattice parameters.

In examination of $\Delta\sigma$, we also adopted a larger number of k-points with a larger cut-off energy and/or rescaling of lattice parameter (*vide infra*).

The magnetic-shielding anisotropy ($\Delta\sigma$) and the magnetic-shielding asymmetry (η) outputted from CASTEP follows the so-called Haeberlen notation [IUPAC]:

$$\Delta\sigma = \sigma_{ZZ} - (\sigma_{XX} + \sigma_{YY})/2, \qquad (2)$$

and

$$\eta = 3(\sigma_{YY} - \sigma_{XX})/2\,\Delta\sigma, \qquad (3)$$

with the three principal components related to the isotropic σ_{iso} as,

$$| \sigma_{ZZ} - \sigma_{iso} | \geq | \sigma_{XX} - \sigma_{iso} | \geq | \sigma_{YY} - \sigma_{iso} |. \qquad (4)$$

For simplicity, we shall refer to magnetic-shielding anisotropy ($\Delta\sigma$) and magnetic-shielding asymmetry (η) as shielding anisotropy and shielding asymmetry, respectively.

3. Results

The crystal structure of TiF_4 is shown in Figure 1 [8]. Three TiF_6 octahedron units share three equatorial bridging fluorines (F5, F9, and F12 in Figure 2) to form a $[Ti_3F_{15}]$-ring. Note here that we use the original F-numbering in Ref. [8]. The rings are connected with each other via the axial bridging fluorines (F1, F2, and F6 in Figure 2) to form an infinite ladder structure along the *b* axis. Hence, there are two kinds of bridging fluorines. We shall refer the former F5, F9, and F12 to as equatorial F_B and the latter F1, F2, and F6 to as axial F_B and denote as F_B^{eq} and F_B^{ax}, respectively. The linearity of these Ti-F-Ti bridges has been ascribed to significant π−donation [17]. The remaining two equatorial fluorines in each TiF_6 octahedron unit are the terminal ones and are referred to as F_T (F3, F4, F7, F8, F10, and F11). The crystal system is *Pnma*, and one of the challenges of this work was to resolve the signals from these 12 fluorines.
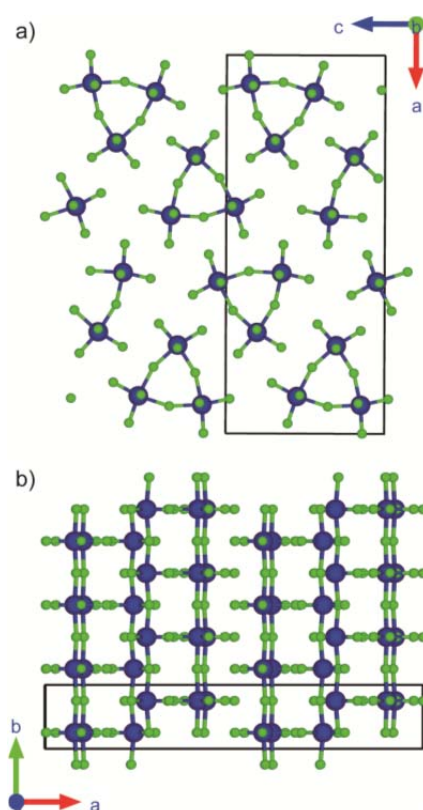

Figure 1. Molecular packing of TiF_4 viewed along the crystallographic *b* axis (a) and along the *c* axis (b) [8]. Larger blue balls are Ti and smaller green ones are F. The unit cell is designated by the solid square.
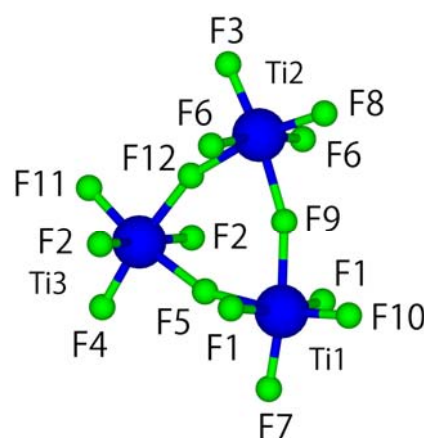

Figure 2. $[Ti_3F_{15}]$-ring [8].

8

Figure 3 shows the observed high-resolution ^{19}F MAS-NMR spectra of solid TiF_4 at the three different magnetic fields. An enlarged plot is given in the Supplementary data (Figure S2). Numerous numbers of spinning sidebands appear in the spectrum taken at 14 T, which led us to employ much lower magnetic fields (4.7 T and 7 T) to identify the isotropic signals. The comparison among the three spectra clearly indicates that those signals designated by the sideways curly brackets at around 0 ppm and 450 ppm are the isotropic signals. It is notable that the latter signals are associated with spinning sidebands spreading over 1000 ppm.
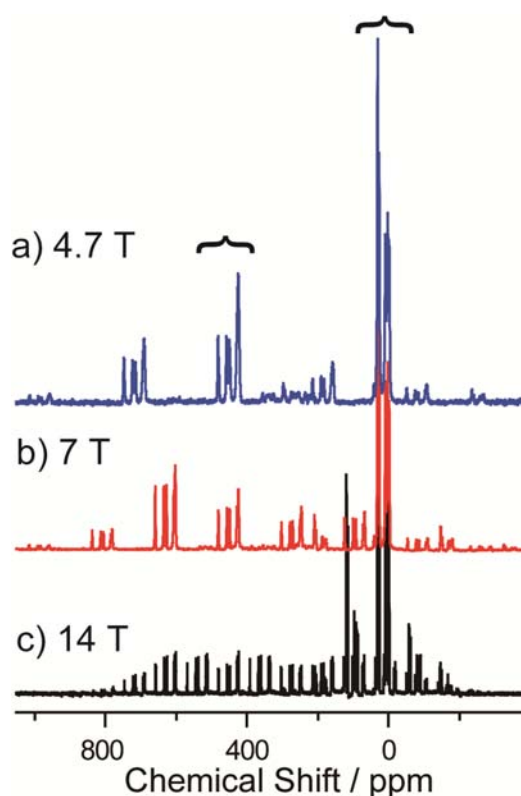

Figure 3. ^{19}F high-resolution MAS NMR spectra of TiF_4 taken at 4.7 T (a), 7 T (b), and 14 T (c) under the MAS frequency of 50 kHz. The isotropic signals at around 0 ppm and 450 ppm are designated by the sideways curly brackets, and the other signals are the spinning sidebands.

As the number of the sidebands increase with increasing the magnetic field strength, we attributed the origin of the observed sidebands to CSA. The size of the ^{19}F-^{19}F dipolar

coupling ($\gamma^2\, \hbar/(2\pi r^3)$) is estimated to be ca. 6.4 kHz for the shortest ^{19}F-^{19}F distance of 0.255 nm in TiF_4, which does not affect the sideband pattern under MAS with ν_R = 50 kHz. Figure 4 is the expanded views of the isotropic signal regions at around 0 and 450 ppm taken at 14 T. The linewidth at the half height was ca. 1 ppm for F4 and 1.5 ppm for F5. Hence, the error for the observed δ_{iso} value is roughly estimate to be ±0.5 ppm. The assignment was done by employing quantum chemical calculation as described in the following.
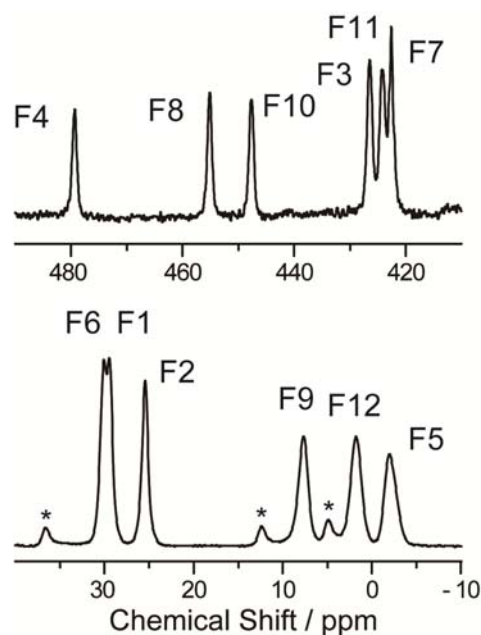

Figure 4. Expanded view of the ^{19}F isotropic signals taken at 14 T (Figure 3c). The isotropic signals are assigned to F1~F12 based on the DFT calculation as described in the text. The signals marked by asterisks denote spinning sidebands.

Sadoc et al. examined ^{19}F NMR parameters in alkali, alkaline earth and rare earth fluorides and found that the isotropic shielding σ_{iso} values obtained by the PBE-DFT GIPAW calculation and the experimental isotropic chemical shift δ_{iso} values are linearly correlated [18]. Further, for compounds having multiple fluorine crystallographic sites, the relative position of the calculated σ_{iso} values are similar to that of the experimental δ_{iso} values. We thus employed the PBE-DFT GIPAW calculation for signal assignment of TiF_4. The observed 12 isotropic signals were assigned to the 12-fluorine sites in TiF_4 by referring the calculated σ_{iso} values as collated with the observed δ_{iso} in Table 1. Further $\Delta\sigma$ and η obtained by spectral fitting of each spinning sideband pattern selectively observed by rs-DANTE

(see below) also collated in Table 1 with the DFT-calculated ones. For ease of comparison, we convert the three components of the chemical-shift tensor (δ_{11}, δ_{22}, δ_{33}) obtained by spectral fitting into $\Delta\sigma$ and η with using Eqs. (2-4). A full list of the principal values (δ_{11}, δ_{22}, δ_{33}) experimentally obtained and the calculated (σ_{XX}, σ_{YY}, σ_{ZZ}) is given in Table S1 of the Supplementary data.

Table 1. Experimental ^{19}F isotropic chemical shift (δ_{iso}) values, calculated isotropic chemical shielding (σ_{iso}) values with $\Delta\sigma$ and asymmetry parameters η.

	Exptl.			Calcd.		
	δ_{iso} / ppm	$\Delta\sigma$ / ppm	η	σ_{iso}/ ppm	$\Delta\sigma$ / ppm	η
F5	-2.0	220.0	0.9	61.2	303.3	0.95
F12	1.7	207.4	0.7	60.5	310.8	0.86
F9	7.6	219.7	0.7	49.5	318.5	0.93
F2	25.4	257.0	0.2	29.0	388.3	0.17
F1	29.4	269.2	0.25	24.3	393.9	0.22
F6	30.0	256.5	0.4	24.2	393.1	0.21
F7	422.5	843.5	0.45	-313.9	906.2	0.44
F11	424.2	831.1	0.45	-314.5	917.0	0.45
F3	426.5	818.8	0.45	-316.0	917.7	0.41
F10	447.7	891.8	0.4	-335.0	952.1	0.39
F8	455.2	879.7	0.45	-356.9	995.6	0.25
F4	479.4	916.6	0.4	-370.9	993.8	0.39

Figure 5a shows linear correlation between the experimental δ_{iso} and the calculated σ_{iso} values, from which we have

$$\delta_{iso} = -(1.13 \pm 0.01)\, \sigma_{iso} + (63 \pm 3), \qquad\qquad (5)$$

with $R^2 = 0.9985$ (error is σ). From Eq. (5), σ_{iso} of the reference compound (CFCl$_3$) is calculated to be 111 ppm. Figure 5b shows correlation among the principal values of the experimental (δ_{11}, δ_{22}, δ_{33}) values and the calculated (σ_{XX}, σ_{YY}, σ_{ZZ}) ones. The straight line through the data points are the linear-regression line, which is written as

$$\delta_{ii} = -(0.94 \pm 0.2)\, \sigma_{kk} + (90 \pm 10), \quad ((i,k) = (1,X), (2,Y), \text{ and } (3,Z)) \quad (6)$$

with $R^2 = 0.9801$. The correlation among the experimental and the calculated ones are good, showing that the PBE-DFT GIPAW calculation is useful for signal assignment.

Figure 5. Correlation between the observed and calculated ^{19}F isotropic chemical shifts (a), and among the experimental (δ_{11}, δ_{22}, δ_{33}) and calculated (σ_{XX}, σ_{YY}, σ_{ZZ}) values (b). In (b), the red, blue, and black crosses denote (δ_{11}, σ_{XX}), (δ_{22}, σ_{YY}), and (δ_{33}, σ_{ZZ}), respectively.

The slope and the y-intercept values in Eq. (5) are different from those reported in Ref. [18] (-(0.80 ± 0.03) and (89 ± 9), respectively). This may be related to the deficient of the PBE-DFT method in describing a 3d localized empty orbital when considering NMR calculation [19]. In fact, Sadoc et al. modified ultrasoft pseudopotential (USPP)
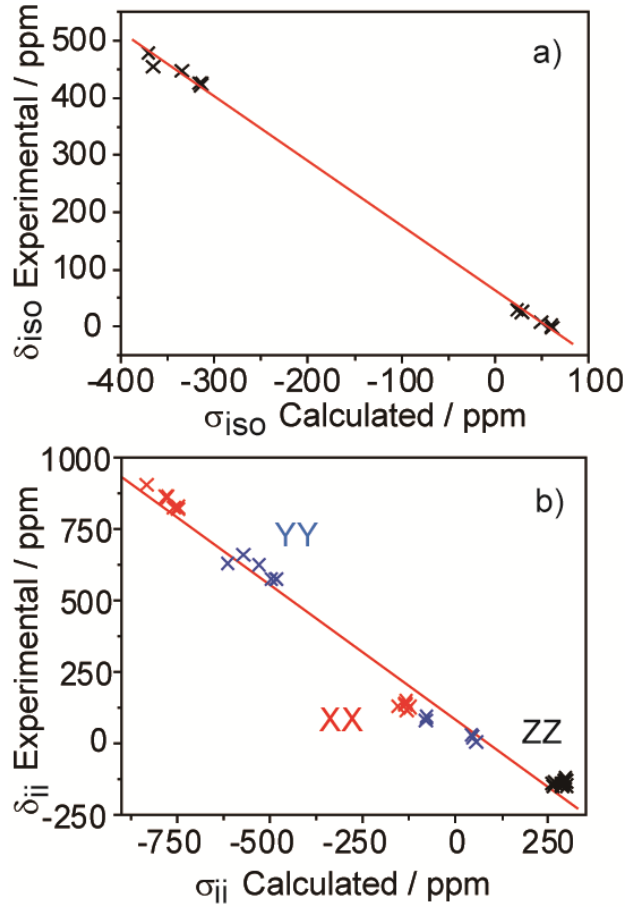
including 3d as well as 4f orbitals for La, Sc, and Ca and found that the modification brings appreciable shift (ca. +26~+40 ppm) in ^{19}F σ_{iso} calculated for LaF_3, ScF_3, and CaF_2 [18]. In this work, however, we have not attempted to, for example, adjust USPP of Ti to realize the Sadoc's relation for TiF_4.

The 6 isotropic signals appearing at 420~480 ppm with the large $\Delta\sigma$ of ~850 ppm are assigned to F_T, that is, the unshared terminal fluorine in the TiF_6-octahedra (F3, F4, F7, F8, F10, and F11). It is noted in Table 1 that the 6 F_T sites can further be classified into two groups; (F4, F8, and F10) and (F3, F7, and F11). The former group appears at 450-480 ppm with larger $\Delta\sigma$ as compared to that for the latter appearing at around 425 ppm. The three signals at around 0 ppm were assigned to F_B^{eq} (F5, F9, and F12) with $\Delta\sigma$ ~ 310 ppm and η ~ 0.9, and those at around 25~30 ppm were F_B^{ax} (F1, F2, and F6) with $\Delta\sigma$ ~ 390 ppm and η ~ 0.2. Correlation between δ_{iso} and $\Delta\sigma$ is also notable, that is, larger $\Delta\sigma$ for larger δ_{iso}.

4. Discussion

Interestingly, the observed high-frequency shift up to ca. 480 ppm for F_T in TiF_4 is the opposite extreme as compared to the observed low-frequency shift of -414.3 ppm for F_T in a palladium (II) fluoride complexes [6]. This suggests wide variation of the electronic state of a terminal fluorine bonded to a transition metal. The observed isotropic chemical shifts for F_T also show high-frequency shift even compared with those in solution. As reviewed by Benjamin et al., it has been shown that TiF_4 dissolves in many common O-donor solvents to form $[TiF_4(L)_2]$, for some of which ^{19}F solution-state NMR results have been reported [17]. In $\{TiF_4(PhCN)\}_3$, the reported chemical shifts were ca. 300 ± 40 ppm for F_T and 0 ± 20 ppm for F_B [20]. Somewhat averaged values of these two were reported for TiF_4 complexes with EtOH and H_2O; 73.4 ppm for $[TiF_6]^{2-}$, 190.1 and 129.9 ppm for $TiF_4 \cdot 2H_2O$ [21]. For $TiF_4 \cdot DME$ (1,2-dimethoxyethane), δ_{iso} were 154 and 238 ppm [22]. Slightly higher frequency shifts were reported for $TiF_{4-x}Cl_x$ as $\delta_{iso} = 160 \sim 300$ ppm [23]. These show that the observed δ_{iso} values for F_T in solution are appreciably smaller than those observed for TiF_4 in solids.

For chemical shielding of a ^{19}F spin, two terms with opposite signs have to be considered [24,25]. One is the conventional "shielding" term, that is, the first-order term corresponding to the opposite field against the external magnetic field produced by electrons surrounding ^{19}F. Note that this diamagnetic shielding causes a low-frequency shift. The second-order "paramagnetic" term comes from the excitation of p-electrons by the external field, which may be written as [24-26]

$$\delta_{para} \sim < \Phi occ \mid \mathbf{L} \mid \Phi vac >< \Phi vac \mid \mathbf{L}_N/r^3 \mid \Phi occ > / \Delta E, \quad (7)$$

where Φocc and Φvac are the wave function of the occupied and the vacant orbitals, respectively, $\mathbf{L}$ and $\mathbf{L_N}$ denote angular momentum operators with respect to the magnetic field and nuclear origins, respectively, r is the distance between the nuclear spin and the electron, and ΔE is the energy difference between the occupied and vacant orbitals. We shall simply refer to δ_{para} as the paramagnetic shift here.

It has been long known that the large range of ^{19}F chemical shifts arises mainly from the paramagnetic term. In fact, Saika and Slichter showed, by comparing HF ($\delta_{iso} \sim -214$ ppm) and F_2 ($\delta_{iso} \sim 420$ ppm), that the high-frequency shift for F_2 is due to larger second-order paramagnetic effects from valence electrons in F_2 [27]. Similarly, the observed high-frequency shift of for F_T ($\delta_{iso} \sim 450$ ppm) may be ascribable to increased covalency for the Ti-F_T bond, and the low-frequency shift for F_B indicates that the Ti-F_B bond is more ionic. We consider that the low-frequency shift of the TiF_4 compounds in solution can, at least in part, be attributable to increase of the ionic character by dissolution.

Eq. (7) indicates that δ_{para} becomes larger when the distance (r in Eq. (7)) between the valence p-electrons and F nucleus become shorter if the distance does not affect ΔE significantly. To get an immediate appreciation of the effect of r, we examined correlation between the observed ^{19}F isotropic chemical
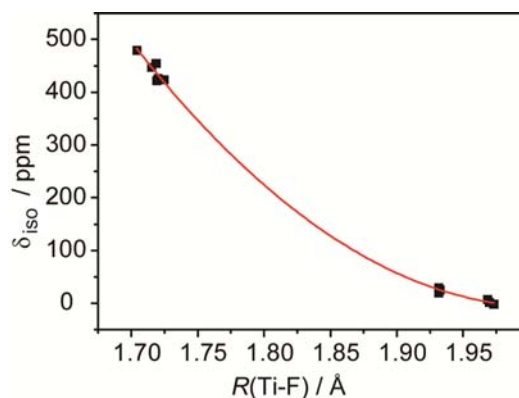

Figure 6. Correlation between the observed ^{19}F isotropic chemical shifts (δ_{iso}) and the bond lengths (R(Ti-F) in Table S1 of the Supplementary data) of the Ti-F direct bond. For F_B^{eq}, we used the average of the two T-F direct bonding lengths for R(Ti-F).

shifts (δ_{iso}) and the bond lengths R(Ti-F) of the Ti-F direct bond (Figure 6). Here, we assumed that r and R are correlated. The Ti-F bond distances are collated in the Supplementary data (Table S2). For eye-guidance, we fitted the data designated by the black square to a quadratic function with δ_{iso} (ppm) = (5.2 ± 0.7) ×10^3×X^2 − (2.1 ± 0.3) ×10^4×X + (2.1 ± 0.2) ×10^4, where $X = R$(Ti-F) (Å). Indeed, the shorter R(Ti-F) leads the shorter r with the higher-frequency shift. Davidovich et al. showed that, for the structurally studied fluorides and oxofluoride complexes of Ti(IV), Ti-F_B bonds are longer than Ti-F_T bonds by ca. 0.2 Å [7].

To appreciate the ionic contributions in the Ti-F bonds, the atomic populations and Mulliken charges were calculated and given in the Supplementary data (Table S2). The negative charges for F_T (ca. -0.48) are smaller than those for F_B (ca. -0.36), indicating weaker electronegative nature for F_T.

For rough estimation of ΔE in Eq. (7), we calculated the partial density of states (DOS), which is shown in the Supplementary data (Figure S3). The expanded view of the valence band plotted in Figure 7(a) shows that the topmost valence band below 0 eV is
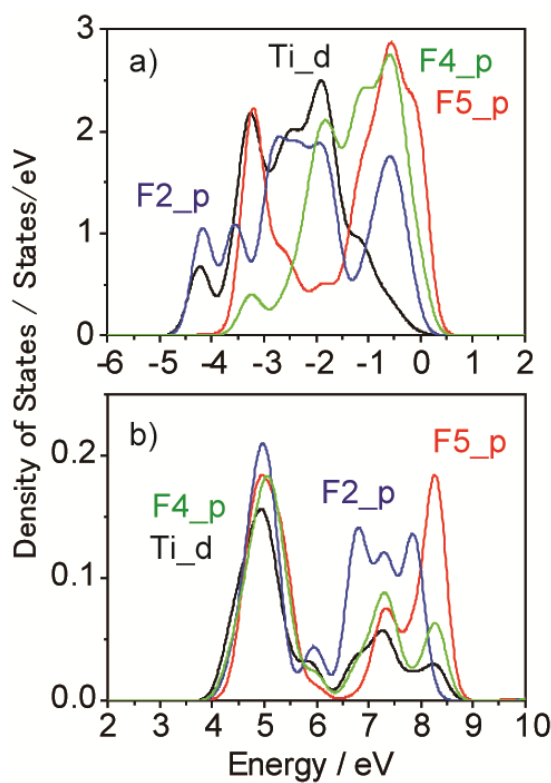

Figure 7. Partial electronic density of states (DOS) of F-p and Ti-d in the valence (a) and the conduction (b) bands, respectively. For ease of comparison, DOS of Ti is divided by 4 in (a) or 400 in (b). Further, DOS of F4 is divided by 2 in (b).

dominated by F-2p, which is attributable to the F⁻ state. Below this band, there exists bands consisted of F-2p and Ti-3d, indicating hybridization of the Ti-3d and F-2p orbitals. Similarly, in the conduction band (Figure 7(b)), the hybridization is appreciable. Especially for F4, better hybridization for the Ti-3d and F4-2p electrons is suggested by the similarity of their DOS curves, which suggests increased covalency for the Ti-F_T bonds. The hybridization of Ti-3d and F-2p will be discussed afterwards with examination of orientations of the shielding tensor relative to the molecular frame. The energies of these hybrid orbitals in the conduction bands are similar among the three fluorine atoms and is E_{con} ~ ca. 5 eV. The energies of the hybrid orbitals in the valence band are different and are in the order of E_{val}(F4) > E_{val}(F2) > E_{val}(F5). Hence, one can estimate the order of ΔE in Eq. (7) as ΔE(F4) < ΔE(F2) < ΔE(F5), which also contributes to the larger high-frequency shift of F4.

To conclude, the larger high-frequency shift for F_T is attributable to the paramagnetic shift enhanced by increased covalency, shorter Ti-F bonds, and smaller energy difference between the occupied and vacant orbitals.

Having discussed the observed isotropic shifts, which are well modeled by PBE-DFT calculation, let us examine the shielding tensor. An ORTEP drawing of the calculated ¹⁹F shielding tensor is
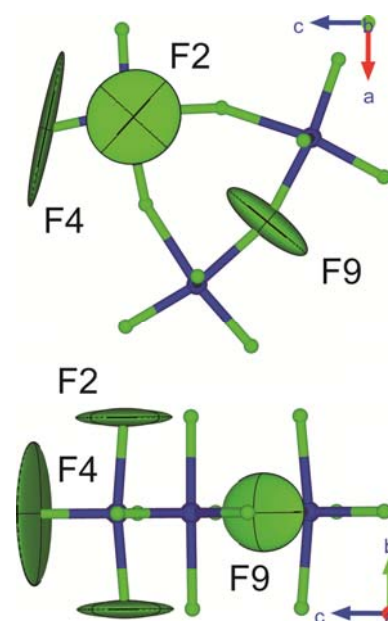

Figure 8. An ORTEP drawing showing the representation of the ¹⁹F chemical-shift tensor deduced for TiF₄ viewed along the crystallographic *b* axis (top) and along the *a* axis (bottom).

represented in Figure 8. For clarity, only three tensors representing F_T (F4), F_B^{ex} (F9), and F_B^{ax} (F2) are drawn as ellipsoids. To appreciate the paramagnetic shift, we adopted an unorthodox representing of the ellipsoid; it is drawn with its longest axes corresponding to the highest-frequency (the most deshielded) component in the shielding tensor. In other words, the longest axis points to the direction at which the paramagnetic shift is most prominent. For all F sites, the paramagnetic shift is significantly reduced along the direction of the Ti-F bond and appears in the plane perpendicular to the Ti-F bond direction.

Eq. (7) indicates that, to produce the paramagnetic shift, the occupied and vacant orbitals must have the appropriate symmetries to undergo magnetic-dipole allowed mixing by the applied magnetic field [26]. The paramagnetic shielding contributions are produced in a direction perpendicular to the plane of mixing. To examine the molecular orbitals of TiF_4, we firstly simplify the problem by considering only the F_T-Ti-F_T moiety in the isolated TiF_6 octahedral unit. Note that both structures belong to the point group C_{2v}. The 6 p-orbitals of F in TiF_2 were grouped into 6 symmetry-adapted orbitals, which were then used to form the Ti-F bond by symmetry-adapted linear combination (SALC) with the $3d$-orbitals of Ti. It is shown that the combination of the d_{YZ} orbital of Ti and p_z of F is suitable for the Ti-F bonding (Figure 9). Details are given in Section S1 in the Supplementary data.

By the simple inspection of Figure 9 and Eq. (7), one can explain the orientation of the shielding tensor as follows. From the illustration schematically showing the orbitals corresponding to Φocc and Φvac, it is clear that the rotation around the z axis (the Ti-F bond direction) does not affect them. Hence, the integration of $< \Phi vac \mid L_z \mid \Phi occ>$ becomes 0, indicating no paramagnetic shift along the Ti-F bond direction. Whereas the 180-degree rotation around x and y would bring $< \Phi vac \mid L_x$ or $L_y \mid \Phi occ> \neq 0$, leading to appreciable paramagnetic shift in the xy plane. The orientation for F_B should also be attributable to the σ bond due to the Ti-3d and F-p hybridization.

In the following, we examine $\Delta\sigma$ and η. As $\Delta\sigma$ in Hz exceeds the spinning frequency ($\nu_R = 50$ kHz), many spinning sidebands appear especially at 14 T. Hence selective observation of each spinning sideband pattern is required for examination. For that, we employed rs-DANTE [9]. All observed sideband patterns for F1~F12 are given in Figure S4 of the Supplementary data. The principal values of the chemical-shift tensor (δ_{11}, δ_{22}, δ_{33}) were deduced by spectral fitting using the program "dmfit" [11]. A full list of the best-fit (δ_{11}, δ_{22}, δ_{33}) and the calculated (σ_{XX}, σ_{YY}, σ_{ZZ}) values is given as Table S2 in the Supplementary data and plotted in Figure 5b.
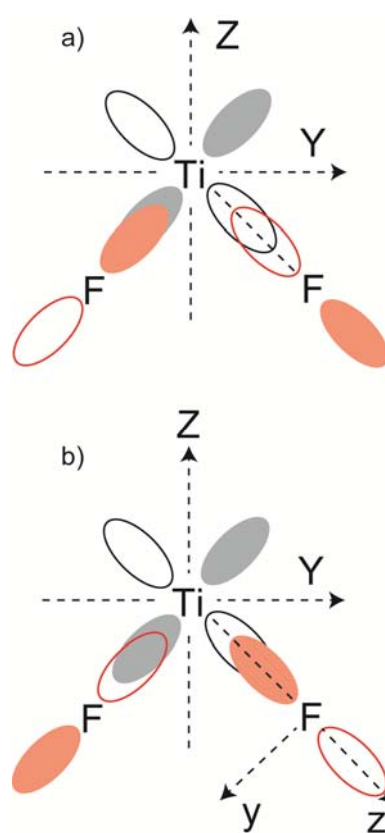

Figure 9. Schematic drawing of SALC MO (bonding (a) and anti-bonding (b)) for the Ti-F bond in the F_T-Ti-F_T moiety. The (X, Y, Z) coordinate is used to describe the TiF$_2$ moiety, while (x, y, z) is to designate the p-orbitals of F by taking the Ti-F bond as the z axis.

The spinning sideband pattern for F4, which bears the largest calculated $\Delta\sigma$ = 993.8 ppm (Table 1), is shown in Figure 10(a). Some signals from F_B^{eq} at around 0 ppm could not be removed, however, these remaining signals do not bother the spectral fitting. The $\Delta\sigma$ and η values calculated from the best-fit (δ_{11}, δ_{22}, δ_{33}) values using Eqs. (2-4) are $\Delta\sigma$ = 916.6 ppm and η = 0.4 and the simulated pattern is given in Figure 10(b). The pattern using the DFT calculated values ($\Delta\sigma$ = 993.8 ppm and η = 0.39 in Table 1) is also shown in Figure 10(c). Although the DFT-calculated $\Delta\sigma$ is ca. 8 % larger than the experimental $\Delta\sigma$, we consider
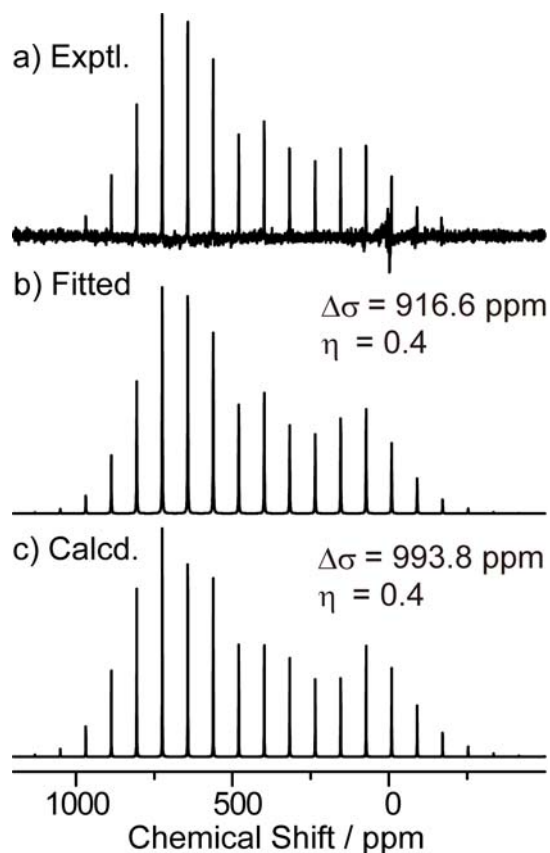

Figure 10. Observed spinning sideband pattern for F4 (a). (b) and (c) are calculated ones using the best-fit parameters (b) and the DFT-calculated ones (c), which are designated in the

that the PBE-DFT GIPAW calculation can be used to model the magnetic shielding of F_T.

In Figure 11, we compare the observed, the fitted, and the calculated patterns for F6 and F9, which represent F_B^{ax} and F_B^{eq}, respectively. The best-fit and DFT-calculated ($\Delta\sigma$, η) values used to calculate the patterns are also shown. It is now apparent that the calculated patterns are inconsistent with those observed for F_B; the DFT-calculated $\Delta\sigma$ values are ca. 45~50 % larger than the experimental $\Delta\sigma$. We naively attributed this to
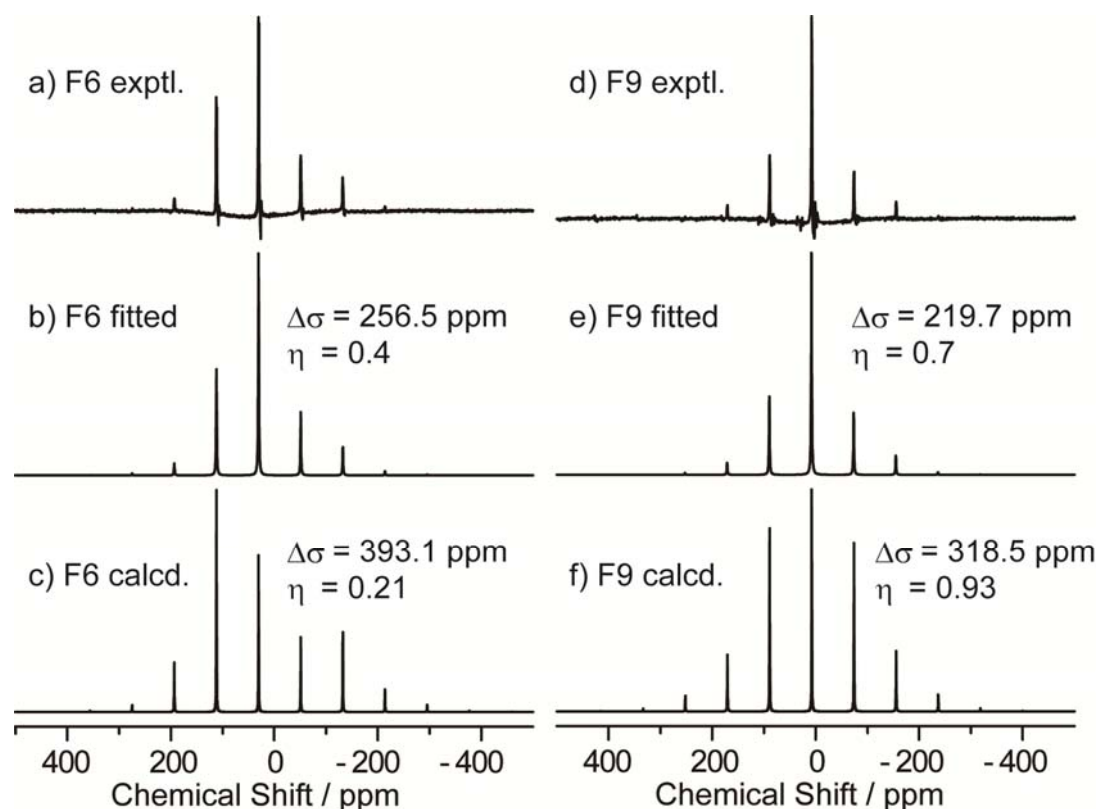
20

Figure 11. Observed spinning sideband patterns for F6 (a) and F9 (d). (b,c,e,f) are calculated ones using the best-fit parameters (b, e) and the DFT-calculated ones (c,f), which are designated in the Figure.

partial averaging of shielding anisotropy by local motion for F_B, and temperature dependence of the ^{19}F high-resolution MAS NMR of TiF_4 were examined. The results (Section S2 in the Supplementary data) indicate that local motion of F_B responsible for reduction of shielding anisotropy is less appreciable for the temperature range studied (-40 ~ 80 °C).

We therefore doubted the adequacy of the parameters/options adopted in the present PBE-DFT calculation, namely, k-points, cut-off energy, and constraints for geometry optimization. Calculated σ_{iso}, $\Delta\sigma$, and η for F4, F6, and F9 under different conditions are collated in Table S3 of the Supplementary data. It is clear that these parameters affect the calculated σ_{iso} values and slightly different slope and y-intercept

21

values for linear correlation between the calculated σ_{iso} and the experimental δ_{iso} were obtained. However for $\Delta\sigma$, none of the increased number of k-points, the larger cut-off energy, and the rescaling of lattice parameters in geometry optimization affect $\Delta\sigma$ significantly. Hence it is clear that the present PBE-DFT calculation in CASTEP is not able to use quantitative prediction of $\Delta\sigma$. Lastly it should be mentioned here that some of these calculations result in the assignment of the peak at 29.4 ppm being F6 and that at 30.0 ppm being F1.

Lastly, we briefly examined effects of modification of USPP. $\Delta\sigma$ and η were calculated with or without a shift of +2.72114 eV (+0.1 E_h) applied on the 3d orbitals of Ti. These calculations were done without geometry optimization. The calculated ($\Delta\sigma$, η) values for F6 without and with the energy shift are (367 ppm, 0.2) and (325 ppm, 0.2), respectively. For F6, (-300 ppm, 0.9) becomes (263 ppm, 0.8) with the energy shift. Certainly by shifting the energy of the Ti 3d orbitals, the magnitude of the calculated $\Delta\sigma$ value is reduced appreciably and comes closer to the experimental one. With a larger energy shift, one may achieve good agreement for F_B. However, the energy shift brought about discrepancy for F_T; for F4, the calculated ($\Delta\sigma$, η) values without and with the energy shift are (994 ppm, 0.4) and (820 ppm, 0.4), respectively. Hence it appears that the observed inconsistency between the calculated and experimental $\Delta\sigma$ values cannot simply be ameliorated by an energy shift of the 3d orbitals of Ti.

5. Summary

In this work, we examined ^{19}F solid-state NMR spectra of TiF$_4$, in which 12 crystallographically and thus magnetically different F sites exist. Half of them (F$_B$) act as bridging ligands between two Ti atoms and the other 6 fluorines are unshared terminal ones (F$_T$). Inspection of the ^{19}F spectra taken at three different magnetic fields shows 12 isotropic signals. Among them, 6 signals appear at around 450 ppm and the others at -5~30 ppm. Further, a large shielding anisotropy $\Delta\sigma \sim 1000$ ppm was suggested for the former. The assignment of these signals were done by employing the PBE-DFT GIPAW calculation. Good linear correlation ($R^2 = 0.9985$) was found between the observed isotropic chemical shifts and the calculated isotropic shielding values. The 6 isotropic signals appearing at 420~480 ppm with the large $\Delta\sigma$ of ~850 ppm are assigned to F$_T$ and the others at -10~30ppm to F$_B$.

The seemingly anomalous ^{19}F isotropic chemical shifts ($\delta_{iso} \sim 450$ ppm and $\Delta\sigma \sim 850$ ppm) for F$_T$ were explained and rationalized in terms of the electronic structure with the Ramsey's equation for the chemical shielding. The large high-frequency of F$_T$ was ascribed to increased covalency of the Ti-F$_T$ bond with the short Ti-F direct bond length (~1.72 Å) and the smaller energy difference between the occupied and vacant orbitals. The calculated chemical-shielding tensors for all fluorines show a common characteristic orientation to the Ti-F bond; the most deshielded tensor component is oriented along the Ti-F bond. This orientation was explained by invoking a Ti-F σ bond formed by d_{YZ} of Ti and p_z of F.

The $\Delta\sigma$ and η values deduced from the spinning sideband pattern selectively observed by using rotation-synchronized DANTE were not consistent with those

calculated ones especially for $\Delta\sigma$ of F_B, indicating deficiency of the present PBE-DFT

calculation in evaluating $\Delta\sigma$.

Acknowledgments

Supplementary data

Supplementary data (PDF) is available, which contains calculated dependence of the isotropic chemical shift and the chemical-shift anisotropy of F4 on the cut-off energy used for the DFT calculation (Figure S1), enlarged plot of Figure 3 (Figure S2), best-fit (δ_{11}, δ_{22}, δ_{33}) and calculated (σ_{11}, σ_{22}, σ_{33}) values for F1~F12 (Table S1), calculated atomic populations and Mulliken charges for F1~F12, and corresponding Ti-F direct bond distances (Table S2), partial electronic density of states (DOS) of F2, F4, F5, and Ti in TiF_4 (Figure S3), Ti-F bonding in TiF_2 under C_{2v} symmetry (Section S1), spinning sideband patterns observed selectively for F1~F12 in TiF_4 by rotation-synchronized DANTE (Figure S4), temperature dependence of ^{19}F high-resolution MAS NMR of TiF_4 (Section S2), calculated σ_{iso}, $\Delta\sigma$, and η for F4, F6, and F9 under different conditions (Table S3), and experimental and optimized cell-lengths (Table S4).

References

[1] Reedijk, J. Formation of Fluoride-Containing Coordination Compounds by Decomposition of Transition-Metal Tetrafluoroborates, *Comm. Inorg. Chem.* **1982**, *1*, 379-389. https://doi.org/10.1080/02603598208078105.

[2] Leblanc, M.; Maisonneuve, V.; Tressaud, A. Crystal Chemistry and Selected Physical Properties of Inorganic Fluorides and Oxide-Fluorides, *Chem. Rev.* **2015**, *115*, 1191−1254, https://doi.org/10.1021/cr500173c.

[3] Reinen, D.; Atanasov, M.; Massa, W. The Binding Properties of Terminal and Bridging Fluoride and of Aqua Ligands - a Semiempirical Vibronic Coupling and DFT Study of Mixed-Ligand Manganese(III) Complexes, *Z. Anorg. Allg. Chem.* **2006**, *632*, 1375-1398. https://doi.org/10.1002/zaac.200500529.

[4] Norel, L.; Darago, L.E.; Le Guennic, B.; Chakarawet, K.; Gonzalez, M.I.; Olshansky, J.H.; Rigaut, S.; Long, J.R.; A Terminal Fluoride Ligand Generates Axial Magnetic Anisotropy in Dysprosium Complexes, *Angew. Chem. Int. Ed.* **2018**, *57*, 1933 −1938. https://doi.org/10.1002/anie.201712139.

[5] Olguín, J.; Bernès, S.; Gasque, L. Fluoride Ion as Ligand and Hydrogen Bond Acceptor: Crystal Structures of Two Dinuclear CuII Complexes Built on a Diazecine Template, *Crystals* **2012**, 2, 1357-1365. https://doi.org/10.3390/cryst2031357.

[6] Huacuja, R.; Herbert, D.E.; Fafard, C.M.; Ozerov, O.V. A terminal palladium fluoride complex supported by an anionic PNP pincer ligand, *J. Fluor. Chem.* **2010**, *131*, 1257-1261. https://doi.org/10.1016/j.jfluchem.2010.07.010.

[7] Davidovich, R.L.; Marinin, D.V.; Stavila, V.; Whitmire, K.H. Structural chemistry of fluoride and oxofluoride complexes of titanium(IV), *Coord. Chem. Rev.* **2015**, *299*, 61-82. https://doi.org/10.1016/j.ccr.2015.04.002.

[8] Müller M.; Müller, B.G. Titanium Tetrafluoride - a Surprising Simple Column Structure, H. Bialowons, *Z. Anorg. Allg. Chem.* **1995**, *621*, 1227-1231. https://doi.org/10.1002/zaac.19956210720.

[9] Caravatti, P.; Bodenhausen, G.; Ernst, R.R. Selective pulse experiments in high-resolution solid state NMR, *J. Magn. Reson.* **1983**, *55*, 88-103. https://doi.org/10.1016/0022-2364(83)90279-2.

[10] Takeda, K. OPENCORE NMR: Open-source core modules for implementing an integrated FPGA-based NMR Spectrometer, *J. Magn. Reson.* **2008**, *192*, 218–229. https://doi.org/10.1016/j.jmr.2008.02.019.

[11] Massiot, D.; Fayon, F.; Capron, M.; King, I.; Le Calvé, S.; Alonso, B.; Durand, J.-O.; Bujoli, B.; Gan, Z.; Hoatson, G. Modelling one- and two-dimensional solid-state NMR spectra, *Magn. Reson. Chem.* **2002**, *40*, 70-76. https://doi.org/10.1002/mrc.984.

[12] Brey, W.S.; Brey, M.L. Fluorine-19 NMR. In *Encyclopedia of Nuclear Magnetic Resonance*; 1996; Vol.3; pp. 2063-2071; Grant, D.M.; Harris R.K., eds.; John Wiley and Sons.

[dataset] [13] Karney, C.F.F. (2015). Nearly optimal coverings of orientation space (Version v1.1). Zenodo. http://doi.org/10.5281/zenodo.32025.

[14] Pickard, C.J.; Mauri, F. All-electron magnetic response with pseudopotentials: NMR chemical shifts, *Phys. Rev. B* **2001**, *63*, 245101 (1-13). https://doi.org/10.1103/PhysRevB.63.245101.

[15] Clark, S.J.; Segall, M.D.; Pickard, C.J.; Hasnip, P.J.; Probert, M.I.J.; Refson, K.; Payne, M.C. First principles methods using CASTEP, *Z. Kristallogr.* **2005**, *220*, 67-570. http://doi.org/10.1524/zkri.220.5.567.65075.

[16] Harris, R.K.; Becker, E.D.; de Menezes, S.M.C, Granger, P.; Hoffman, R.E.; Zilm, K.W. Further conventions for NMR shielding and chemical shifts (IUPAC Recommendations 2008). *Pure Appl. Chem.* **2008**, *80,* 59-84, https://doi.org/10.1351/pac200880010059.

[17] Benjamin, S.L.; Levason, W.; Reid, G. Medium and high oxidation state metal/non-metal fluoride and oxide–fluoride complexes with neutral donor ligands, *Chem. Soc. Rev.* **2013**, *42* 1460-1499. https://doi.org/10.1039/c2cs35263j.

[18] Sadoc, A.; Body, M.; Legein, C.; Biswal, M.; Fayon, F.; Rocquefelte, X.; Boucher, F.; NMR parameters in alkali, alkaline earth and rare earth fluorides from first principle calculations, *Phys. Chem. Chem. Phys.* **2011**, *13*, 18539–18550.

http://doi.org/10.1039/c1cp21253b.

[19] Profeta, M.; Benoit, M.; Mauri, F.; Pickard, C.J.; First-Principles Calculation of the ^{17}O NMR Parameters in Ca Oxide and Ca Aluminosilicates: the Partially Covalent Nature of the Ca-O Bond, a Challenge for Density Functional Theory, *J. Am. Chem. Soc.* **2004**, *126*, 12628–12635. http://doi.org/10.1021/ja0490830.

[20] Nikiforov, G.B.; Knapp, C.; Passmore, J.; Decken, A. Interaction of TiF_4 with the donor solvents SO_2, PhCN, and MeCN Isolation and structural characterization of the first trimeric fluorine bridged donor–acceptor adduct $\{TiF_4(PhCN)\}_3$, *J. Fluor. Chem.* **2006**, *127*, 1398–1404. https://doi.org/10.1016/j.jfluchem.2006.05.022.

[21] Nobrega, C.B.C.; Fujiwara, F.Y.; Cury, J.A.; Rosalen, P.L. TiF_4 Varnish − A ^{19}F-NMR Stability Study and Enamel Reactivity Evaluation, *Chem. Pharm. Bull.* **2008**, *56*, 139—141. https://doi.org/10.1248/cpb.56.139.

[22] Borden, R.S.; Loeffler, P.A.; Dyer, D.S. Stereochemistry of Octahedral Titanium(IV) Complexes. II. The Titanium Tetrachloride-Titanium Tetrafluoride-l,2-Dimethoxyethane System, *Inorg. Chem.* **1972**, *11*, 2481-2484. https://doi.org/10.1021/ic50116a037.

[23] Fields, R. Fluorine-19 Nuclear Magnetic Resonance Spectroscopy, *Ann. Rep. NMR Spectrosc.* **1972**, *5A*, 99-304. https://doi.org/10.1016/S0066-4103(08)60436-6.

[24] Ramsey, N.F. Magnetic Shielding of Nuclei in Molecules, *Phys. Rev.* **1950**, *78*, 699-703. https://doi.org/10.1103/PhysRev.78.699.

[25] Ramsey, N.F. Chemical Effects in Nuclear Magnetic Resonance and in Diamagnetic Susceptibility, *Phys. Rev*. **1952**, *86*, 243-246. https://doi.org/10.1103/PhysRev.86.243.

[26] Widdifield, C.M.; Schurko, R.W. Understanding Chemical Shielding Tensors Using Group Theory, MO Analysis, and Modern Density-Functional Theory, *Concepts in Magn. Reson.* A **2009**, *34*, 91-123. https://doi.org/10.1102/cmr.a.20136.

[27] Saika, A.; Slichter, C.P. A Note on the Fluorine Resonance Shifts, *J. Chem. Phys.* **1954**, *22*, 26-28. https://doi.org/10.1063/1.1739849.

[28] Momma, K.; Izumi, F. VESTA 3 for Three-Dimensional Visualization of Crystal, Volumetric and Morphology Data, *J. Appl. Crystallogr.* **2011**, *44*, 1272-1276. https://doi.org/10.1107/S0021889811038970.

Supplementary data

Terminal and Bridging Fluorine Ligands in TiF$_4$ as Studied by ^{19}F NMR in Solids

Miwa Murakami [a*], Yasuto Noda [b], and K. Takegoshi [b]

[a]Office of Society-Academia Collaboration for Innovation, Kyoto University, Gokasho, Uji, Kyoto, 611-0011, Japan.

[b]Graduate School of Science, Kyoto University, Kitashirakawa Oiwakecho, Sakyo-ku, Kyoto, 606-8502, Japan.

[*] email m-murakami@saci.kyoto-u.ac.jp

Contents

Figure S1. Calculated dependence of (a) the isotropic chemical shift and (b) the chemical-shift anisotropy of F4 on the cut-off energy used for the DFT calculation.

Figure S2. Enlarged plot of Figure 3 in the text.

Table S1. Best-fit (δ_{11}, δ_{22}, δ_{33}) and calculated (σ_{XX}, σ_{YY}, σ_{ZZ}) values for F1~F12.

Table S2. Calculated atomic populations and Mulliken charges for F1~F12, and corresponding Ti-F direct bond distances in TiF_4.

Figure S3. Partial electronic density of states (DOS) of F2, F4, F5, and Ti in TiF_4.

Section S1. Ti-F bonding in TiF_2 under C_{2v} symmetry.

Figure S4. Spinning sideband patterns observed selectively for F1~F12 in TiF_4 by rotation-synchronized DANTE.

Section S2. Temperature dependence of ^{19}F high-resolution MAS NMR of TiF_4.

Table S3. Calculated σ_{iso}, $\Delta\sigma$, and η for F4, F6, and F9 under different conditions.

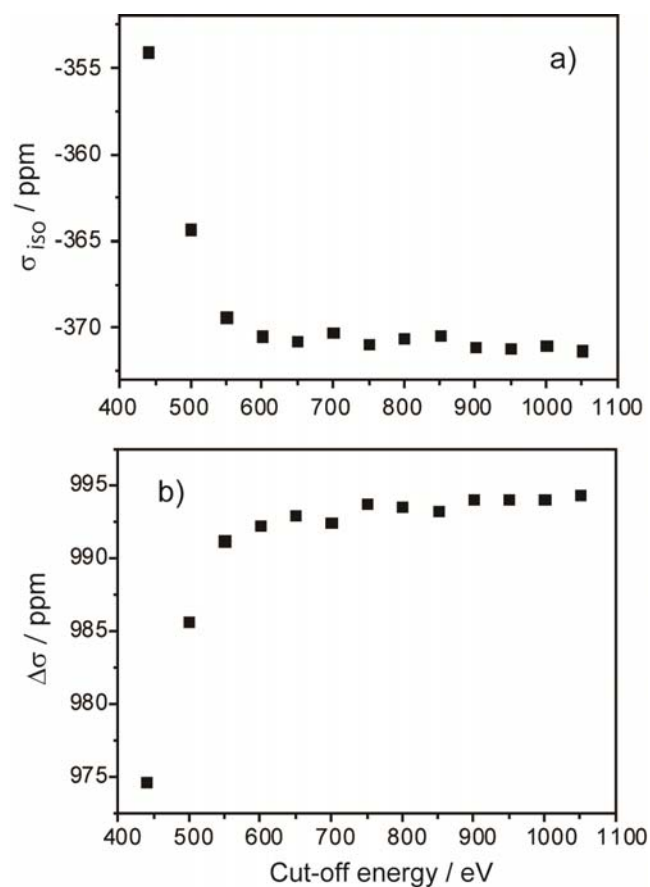Table S4. Experimental and optimized cell-lengths

Figure S1. Calculated dependence of (a) the isotropic chemical shift and (b) the chemical-shift anisotropy ($\Delta\sigma$) of F4 and the cut-off energy used for the calculation. Clearly the cutoff energy larger than 600 eV is desirable. For the asymmetry parameters η, similar results were obtained (not shown).

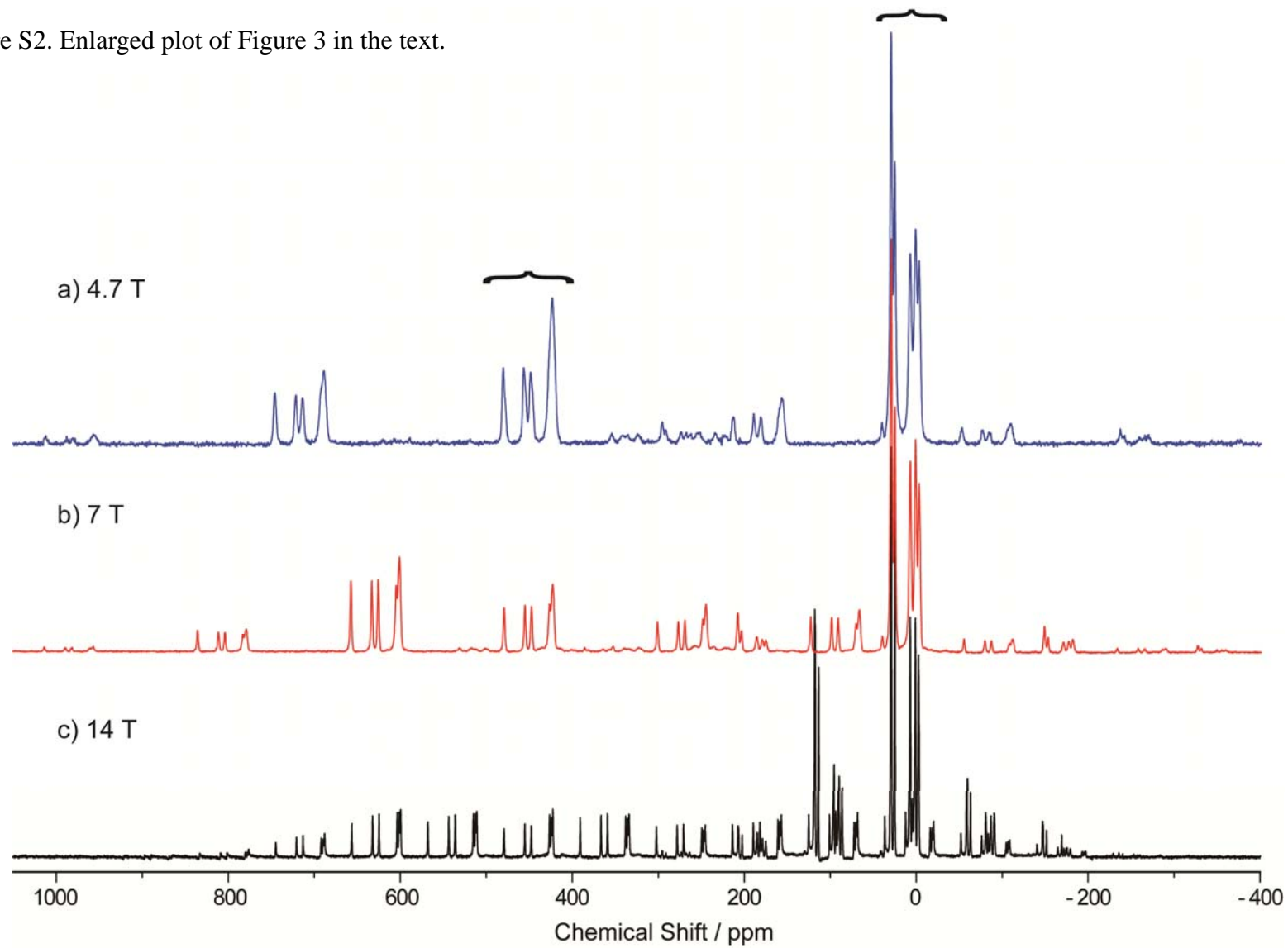Figure S2. Enlarged plot of Figure 3 in the text.

Table S1. Best-fit (δ_{11}, δ_{22}, δ_{33}) and calculated (σ_{XX}, σ_{YY}, σ_{ZZ}) values for F1~F12.[a]

	Exptl.	Sideband fitting					DFT-calculated (Calc-1 in Table S3)					
	δ_{iso}	δ_{11}	δ_{22}	δ_{33}	$\Delta\sigma$	η	σ_{iso}	σ_{XX}	σ_{YY}	σ_{ZZ}	$\Delta\sigma$	η
F1	29.4	141.6	96.7	-150.1	269.2	0.25	21.3	-135.5	-78.6	286.9	393.9	0.22
F2	25.4	128.2	93.9	-145.9	257.0	0.2	29.0	-122.8	-78.0	287.8	388.2	0.17
F3	426.5	822.3	576.1	-119.4	818.8	0.45	-316.0	-747.6	-496.3	295.7	917.7	0.41
F4	479.4	907.2	662.7	-131.7	916.6	0.4	-370.9	-832.8	-571.6	291.6	993.8	0.39
F5	-2.0	137.3	5.3	-148.7	220.0	0.9	61.2	-135.8	56.0	263.4	303.3	0.95
F6	30.0	149.7	81.3	-141.0	256.5	0.4	24.2	-133.8	-80.0	286.2	393.1	0.21
F7	422.5	830.2	577.1	-139.8	843.5	0.45	-313.9	-748.6	-483.1	290.2	906.2	0.44
F8	455.2	865.7	631.1	-131.3	879.7	0.45	-365.9	-781.1	-614.4	297.8	995.6	0.25
F9	7.6	132.1	29.6	-138.9	219.7	0.7	49.5	-155.7	42.4	261.8	318.5	0.93
F10	447.7	863.9	626.1	-146.9	891.8	0.4	-335.0	-775.3	-529.4	299.7	952.1	0.38
F11	424.2	825.9	576.6	-129.9	831.1	0.45	-314.5	-758.4	-482.0	296.8	917.0	0.45
F12	1.7	119.2	22.4	-136.6	207.4	0.7	60.5	-132.5	46.2	267.6	310.8	0.86

[a]All values except for η are given in ppm.

Table S2. Calculated atomic populations and Mulliken charges for F1~F12, and corresponding Ti-F direct bond distances in TiF$_4$.

	s	p	Charge / eV	R(Ti-F) / Å
F5	1.94	5.55	-0.49	1.97
F12	1.94	5.55	-0.49	1.97
F9	1.94	5.54	-0.49	1.97
F2	1.94	5.53	-0.47	1.93
F1	1.94	5.52	-0.47	1.93
F6	1.94	5.52	-0.46	1.93
F11	1.96	5.41	-0.37	1.72
F7	1.96	5.42	-0.37	1.72
F3	1.96	5.41	-0.37	1.72
F10	1.96	5.40	-0.36	1.72
F8	1.96	5.40	-0.36	1.72
F4	1.96	5.39	-0.35	1.70
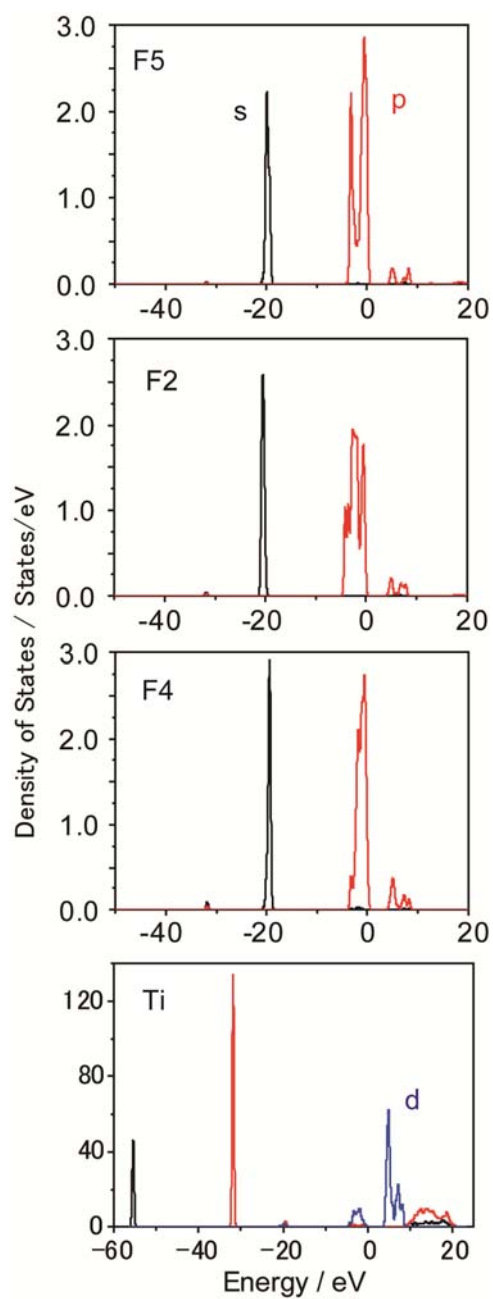
Figure S3. Partial electronic density of states (DOS) of F5, F2, F4, and Ti in TiF$_4$.

Section S1. Ti-F bonding in TiF_2 under C_{2v} symmetry.

Here we simplify the problem by considering only one TiF_6 octahedral unit (Figure 1(a)). It is apparent that the TiF_6 octahedral unit is in the point group C_{2v}. By noting the F_T-Ti-F_T moiety (Figure 1(b)) also belong to C_{2v}, we further simplify the problem by limiting to the F_T-Ti-F_T moiety. The C_2 axis is taken as the Z axis, the σ_v plane is the XZ plane, and $\sigma_{v'}$ is ZY. We also introduce the (x,y,z) axis to designate the p-orbitals of F.

The six p-orbitals for the two fluorines are grouped into the six symmetry-related orbitals with reducible representation being $\Gamma = 2A_1 + A_2 + B_1 + 2B_2$, which are schematically drawn in Figure 2.
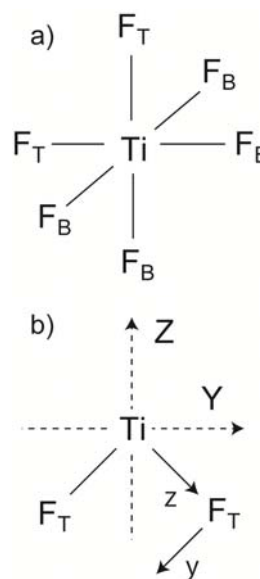
Figure 1. Illustrations of an isolated TiF_6 octahedron unit and the F_T-Ti-F_T moiety.
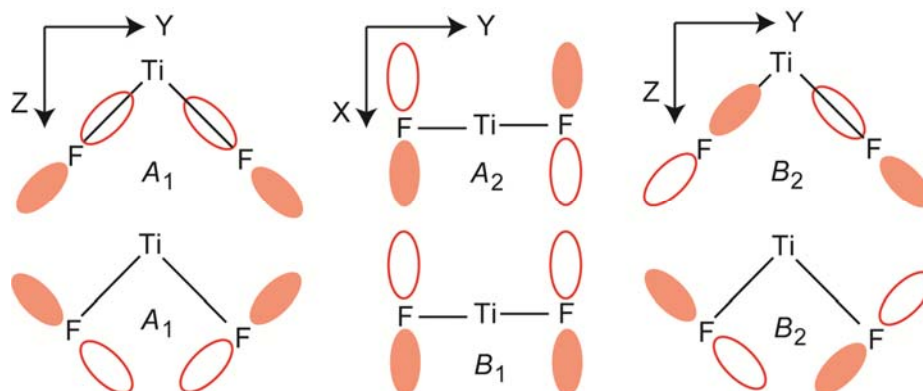
Figure 2. 6 symmetry-adapted orbitals for the two fluorines in TiF_2.

The reducible representation of Ti is $\Gamma = A_1 + B_1 + B_2$, which can directly be related to the 3d electron orbital of Ti as d_Z^2, d_{XZ}, and d_{YZ} for A_1, B_1, and B_2, respectively.

To form a Ti-F bond, we apply symmetry-adapted linear combination (SALC) with the 3d-orbitals of Ti and the p-orbitals in Figure 2. It is clear that the combination of the d_{YZ} orbital of Ti and p_z of F is suitable for formation of the Ti-F bonding (Figure 3).
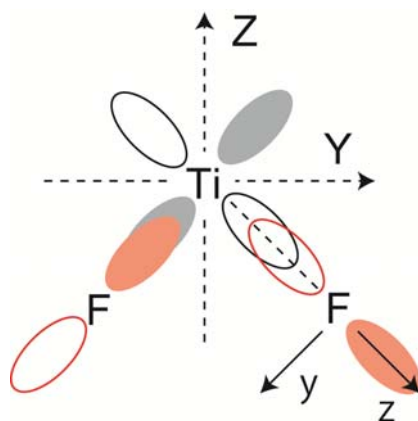
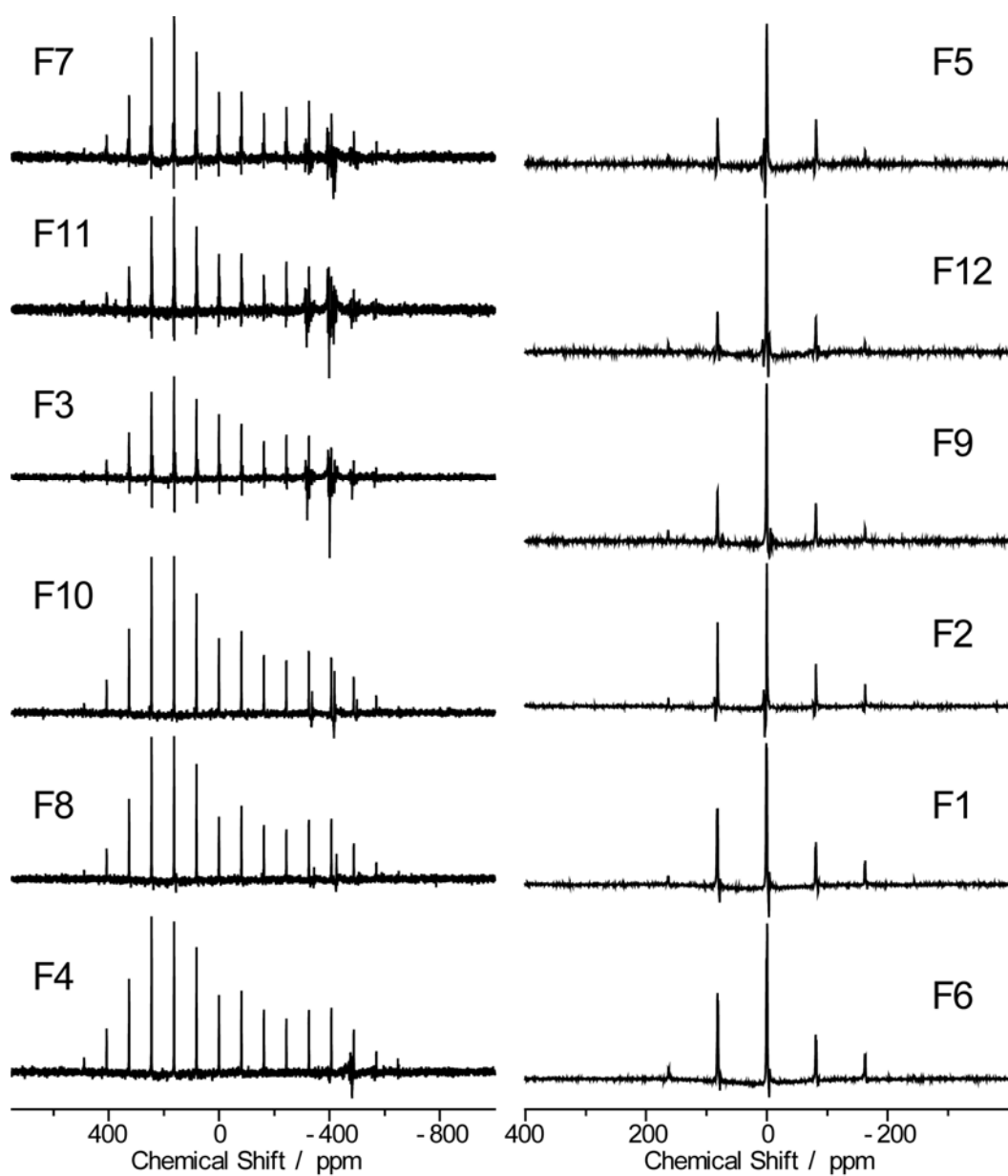Figure 3. Schematic drawing of SALC MO for the Ti-F bond in the F_T-Ti-F_T moiety.

Figure S4. Spinning sideband patterns observed selectively for F1~F12 in TiF_4 by rotation-synchronized DANTE.

Section S2. Temperature dependence of ^{19}F high-resolution MAS NMR of TiF$_4$.

Temperature dependence of ^{19}F high-resolution MAS NMR spectra of TiF$_4$ was observed by using a triply-tuned MAS probe (Agilent) for a 1.6 mm rotor at 14 T (the ^{19}F resonance frequency was 564.8 MHz) using a JEOL ECA600 NMR spectrometer. The ^{19}F MAS spectra were observed by using the Hahn echo sequence under the MAS spinning frequency (ν_R) of 35 kHz. The $\pi/2$ and π pulse lengths were 1.5 µs and 2.8 µs, respectively. The pulse length (t_p) and the number of the short pulse for rs-DANTE were 0.5 µs and 33, respectively. The pulse spacing (Δ) was set as $\Delta = 1/\nu_{MAS}$ - $t_p = 28.1$ µs. The temperature-calibration experiment was done using ^{207}Pb NMR of Pb(NO$_3$)$_2$ [S1].

Figures 4 and 5 show expanded views of the ^{19}F isotropic signals at different temperatures. For the F$_B$ signals, their isotropic shifts increase with increasing temperature, and their linewidths are almost temperature independent (Figure S5). For F$_T$, in addition to the line shift, line broadening is appreciable at both higher and lower temperatures. The broadening at lower temperature may be attributable to distribution of local structure around F$_T$, which, with increasing temperature, is averaged by motion of F$_T$. At higher temperature, the motional frequency reached to the MAS frequency, leading to broadening due to reintroduction of CSA by interference between MAS averaging and molecular motion [S2]. Note that the atomic displacement factors reported in Ref. S3 are slightly larger for F$_T$, which is consistent with the present NMR observation.
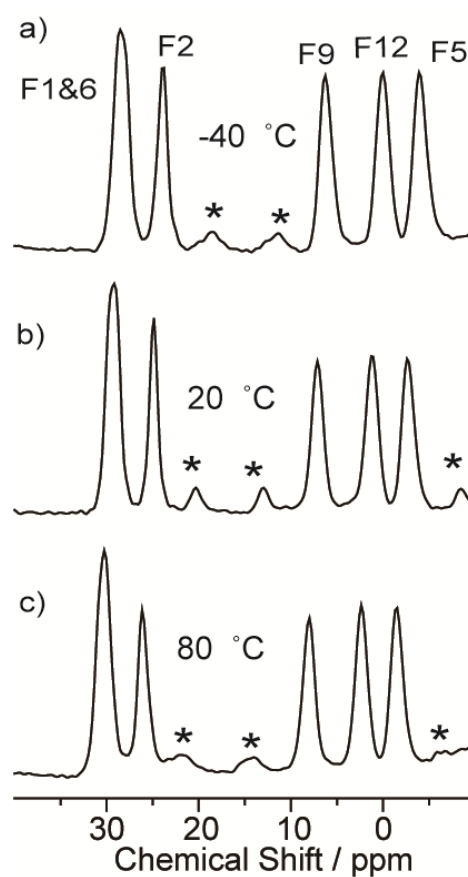

Figure 4. Expand view of the ^{19}F isotropic signals of F$_B$ at (a) -40 ˚C, (b) 20 ˚C, and (c) 80 ˚C. The signals marked by asterisks denote spinning sidebands of F$_T$.

Figures 6 and 7 are observed spinning sideband patterns for F9 (Figure 6) and F10 (Figure 7). Due to the signal overlap brought about by signal broadening, there are many unwanted signal components for the F10 patterns. These spectra indicate clearly that the discrepancy between the observed chemical shift anisotropy and the DFT-calculated ones for F_B is not attributable to motional averaging.
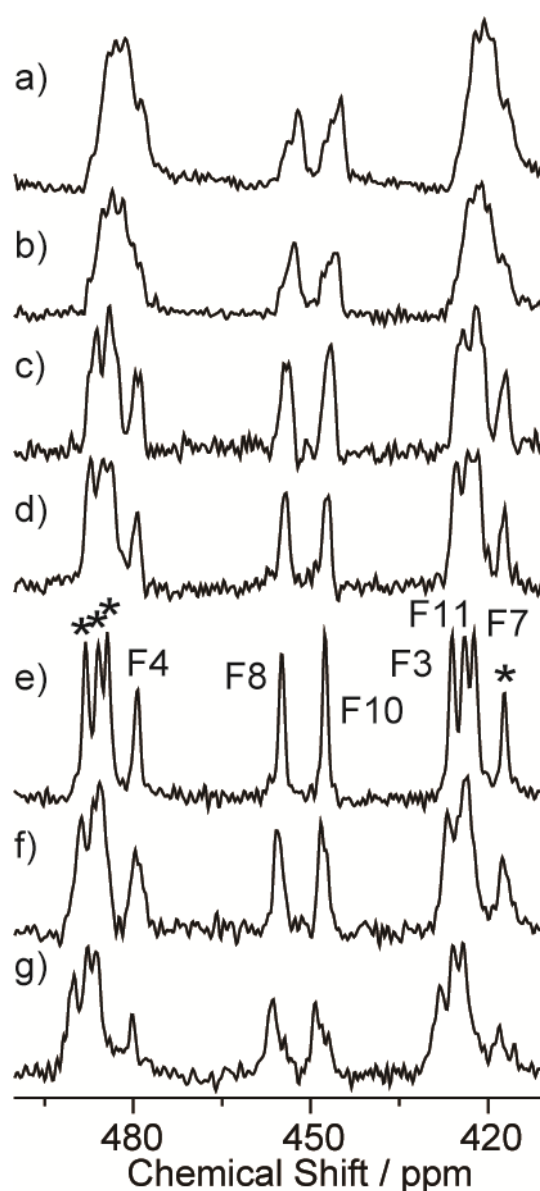

Figure 5. Expand view of the ^{19}F isotropic signals of F_T at (a) -40 ˚C, (b) -20 ˚C, (c) 0 ˚C, (d) 20 ˚C, (e) 40 ˚C, (f) 60 ˚C, and (g) 80 ˚C. The signals marked by asterisks denote spinning sidebands of F_T.
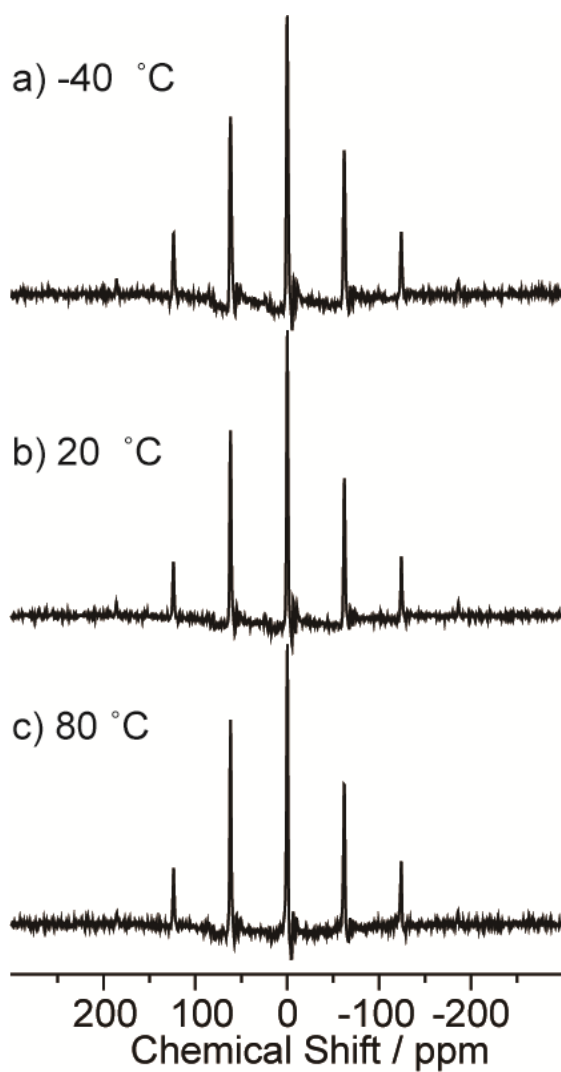
Figure 6. Observed spinning sideband patterns for F9 at (a) -40 ˚C, (b) 20 ˚C, and (c) 80 ˚C. The isotropic signal position is taken as the reference (0 ppm).
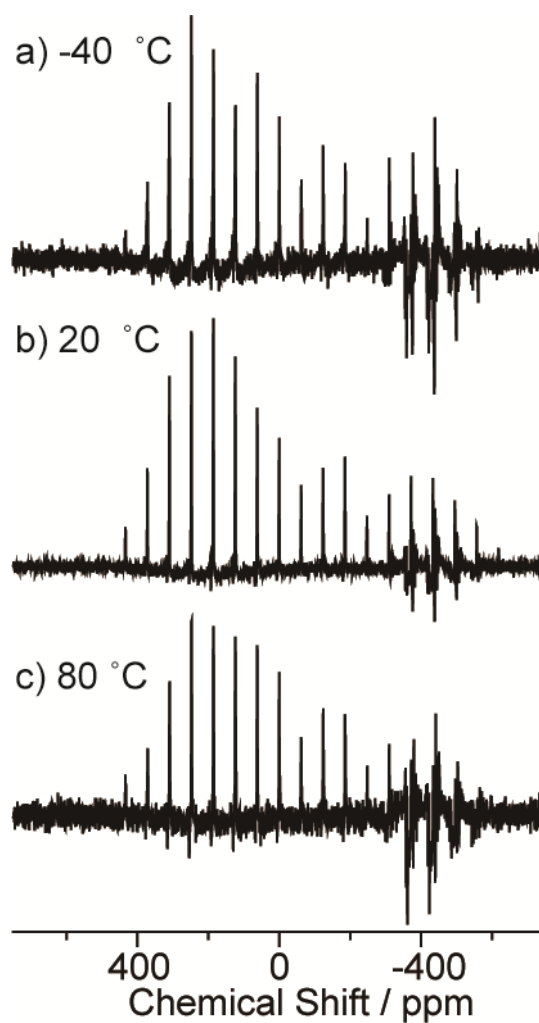
Figure 7. Observed spinning sideband patterns for F10 at (a) -40 ˚C, (b) 20 ˚C, and (c) 80 ˚C. The isotropic signal position is taken as the reference (0 ppm).

Table S3. Calculated σ_{iso}, $\Delta\sigma$, η, for F4, F6, and F9 under different conditions for calculation. Slope, *y*-intercept, and R^2 for linear correlation between the experimental δ_{iso} are also collated.

Calc-#	Rescaling of **l**attice parameters	k-points	Cutoff Energy / eV	F4 σ_{iso} / ppm $\Delta\sigma$ / ppm η	F6 σ_{iso} / ppm $\Delta\sigma$ / ppm η	F9 σ_{iso} / ppm $\Delta\sigma$ / ppm η	Fitting Slope *y*-intercept R^2
1	no	1×4×1	750	-370.9 993.8 0.39	24.2 393.1 0.21	49.5 318.5 0.93	-1.13 ± 0.01 63 ± 3 0.9985
2	no	2×9×4	750	-366.1 989.1 0.42	22.9 395.1 0.21	48.6 319.6 0.9	-1.15 ± 0.01 61 ± 1 0.9997
3	no	2×9×4	850	-366.3 989.6 0.41	23.0 395.3 0.21	48.8 319.5 0.9	-1.15 ± 0.01 61 ± 2 0.9997
4	yes (Table S4)	2×9×4	750	-362.5 987.3 0.44	27.8 394.2 0.22	54.4 320.4 0.92	-1.10 ± 0.01 62 ± 3 0.9989
5	yes (Table S4)	2×13×15	750	-360.9 985.0 0.44	27.7 394.2 0.22	54.7 320.2 0.92	-1.10 ± 0.01 63 ± 3 0.9986

Table S4. Experimental and optimized lattice parameters

	a / Å	*b* / Å	*c* / Å
X-ray diffraction[a]	22.81	3.848	9.568
Calc-4	24.88	3.909	10.18
Calc-5	24.74	3.908	10.24

[a]Ref. [S3]

References

[S1] Bielecki, A.; Brum, D.P. Temperature Dependence of ^{207}Pb MAS Spectra of Solid Lead Nitrate. An Accurate, Sensitive Thermometer for Variable-temperature MAS. *J. Magn. Reson. A* **1995**, *116*, 215-220. https://doi.org/10.1006/jmra.1995.0010

[S2] Suwelack, D.; Rothwell, W.P.; Waugh, J.S. Slow molecular motion detected in the NMR spectra of rotating solids. *J. Chem. Phys.* **1980**, 73, 2559-2569. https://doi.org/10.1063/1.440491

[S3] Müller M.; Müller, B.G. Titanium Tetrafluoride - a Surprising Simple Column Structure, H. Bialowons, *Z. Anorg. Allg. Chem.* **1995**, *621*, 1227-1231. https://doi.org/10.1002/zaac.19956210720.